

CERN-PH-EP-2015-085

30 March 2015

The Spin Structure Function g_1^p of the Proton and a Test of the Bjorken Sum Rule

The COMPASS Collaboration

Abstract

New results for the double spin asymmetry A_1^p and the proton longitudinal spin structure function g_1^p are presented. They were obtained by the COMPASS collaboration using polarised 200 GeV muons scattered off a longitudinally polarised NH_3 target. The data were collected in 2011 and complement those recorded in 2007 at 160 GeV, in particular at lower values of x . They improve the statistical precision of $g_1^p(x)$ by about a factor of two in the region $x \lesssim 0.02$. A next-to-leading order QCD fit to the g_1 world data is performed. It leads to a new determination of the quark spin contribution to the nucleon spin, $\Delta\Sigma$ ranging from 0.26 to 0.36, and to a re-evaluation of the first moment of g_1^p . The uncertainty of $\Delta\Sigma$ is mostly due to the large uncertainty in the present determinations of the gluon helicity distribution. A new evaluation of the Bjorken sum rule based on the COMPASS results for the non-singlet structure function $g_1^{\text{NS}}(x, Q^2)$ yields as ratio of the axial and vector coupling constants $|g_A/g_V| = 1.22 \pm 0.05$ (stat.) ± 0.10 (syst.), which validates the sum rule to an accuracy of about 9%.

Keywords: COMPASS; deep inelastic scattering; spin; structure function; QCD analysis; parton helicity distributions; Bjorken sum rule.

(to be submitted to *Phys. Lett. B*)

The COMPASS Collaboration

C. Adolph⁹, R. Akhunzyanov⁸, M.G. Alexeev²⁸, G.D. Alexeev⁸, A. Amoroso^{28,29}, V. Andrieux²², V. Anosov⁸, A. Austregesilo¹⁷, C. Azevedo², B. Badetek³², F. Balestra^{28,29}, J. Barth⁵, G. Baum^a, R. Beck⁴, Y. Bedfer^{22,11}, J. Bernhard^{14,11}, K. Bicker^{17,11}, E. R. Bielert¹¹, R. Birsa²⁶, J. Bisplinghoff⁴, M. Bodlak¹⁹, M. Boer²², P. Bordalo^{13,b}, F. Bradamante^{25,26}, C. Braun⁹, A. Bressan^{25,26}, M. Büchele¹⁰, E. Burtin²², L. Capozza^{22,c}, W.-C. Chang²³, M. Chiosso^{28,29}, I. Choi³⁰, S.U. Chung^{17,d}, A. Cicuttin^{27,26}, M.L. Crespo^{27,26}, Q. Curiel²², S. Dalla Torre²⁶, S.S. Dasgupta⁷, S. Dasgupta^{25,26}, O.Yu. Denisov²⁹, L. Dhara⁷, S.V. Donskov²¹, N. Doshita³⁴, V. Duic²⁵, M. Dziewiecki³³, A. Efremov⁸, P.D. Eversheim⁴, W. Eyrich⁹, A. Ferrero²², M. Finger¹⁹, M. Finger jr.¹⁹, H. Fischer¹⁰, C. Franco¹³, N. du Fresne von Hohenesche¹⁴, J.M. Friedrich¹⁷, V. Frolov^{8,11}, E. Fuchey²², F. Gautheron³, O.P. Gavrichtchouk⁸, S. Gerassimov^{16,17}, F. Giordano³⁰, I. Gnesi^{28,29}, M. Gorzelli¹⁰, S. Grabmüller¹⁷, A. Grasso^{28,29}, M. Grosse-Perdekamp³⁰, B. Grube¹⁷, T. Grussenmeyer¹⁰, A. Guskov⁸, F. Haas¹⁷, D. Hahne⁵, D. von Harrach¹⁴, R. Hashimoto³⁴, F.H. Heinsius¹⁰, F. Herrmann¹⁰, F. Hinterberger⁴, N. Horikawa^{18,f}, N. d'Hose²², C.-Yu Hsieh²³, S. Huber¹⁷, S. Ishimoto^{34,g}, A. Ivanov⁸, Yu. Ivanshin⁸, T. Iwata³⁴, R. Jahn⁴, V. Jary²⁰, P. Jörg¹⁰, R. Joosten⁴, E. Kabuß¹⁴, B. Ketzer^{17,h}, G.V. Khaustov²¹, Yu.A. Khokhlov^{21,i}, Yu. Kisselev⁸, F. Klein⁵, K. Klimaszewski³¹, J.H. Koivuniemi³, V.N. Kolosov²¹, K. Kondo³⁴, K. Königsmann¹⁰, I. Konorov^{16,17}, V.F. Konstantinov²¹, A.M. Kotzinian^{28,29}, O. Kouznetsov⁸, M. Krämer¹⁷, P. Kremser¹⁰, F. Krinner¹⁷, Z.V. Kroumchtein⁸, N. Kuchinski⁸, F. Kunne²², K. Kurek³¹, R.P. Kurjata³³, A.A. Lednev²¹, A. Lehmann⁹, M. Levillain²², S. Levorato²⁶, J. Lichtenstadt²⁴, R. Longo^{28,29}, A. Maggiora²⁹, A. Magnon²², N. Makins³⁰, N. Makke^{25,26}, G.K. Mallot¹¹, C. Marchand²², A. Martin^{25,26}, J. Marzec³³, J. Matousek¹⁹, H. Matsuda³⁴, T. Matsuda¹⁵, G. Meshcheryakov⁸, W. Meyer³, T. Michigami³⁴, Yu.V. Mikhailov²¹, Y. Miyachi³⁴, A. Nagaytsev⁸, T. Nagel¹⁷, F. Nerling¹⁴, D. Neyret²², V.I. Nikolaenko²¹, J. Novy^{20,11}, W.-D. Nowak¹⁰, A.S. Nunes¹³, A.G. Olshevsky⁸, I. Orlov⁸, M. Ostrick¹⁴, D. Panzieri^{1,29}, B. Parsamyan^{28,29}, S. Paul¹⁷, J.-C. Peng³⁰, F. Pereira², M. Pesek¹⁹, D.V. Peshekhonov⁸, S. Platchkov²², J. Pochodzalla¹⁴, V.A. Polyakov²¹, J. Pretz^{5,j}, M. Quaresma¹³, C. Quintans¹³, S. Ramos^{13,b}, C. Regali¹⁰, G. Reicherz³, C. Riedl³⁰, E. Rocco¹¹, N.S. Rossiyskaya⁸, D.I. Ryabchikov²¹, A. Rychter³³, V.D. Samoylenko²¹, A. Sandacz³¹, C. Santos²⁶, S. Sarkar⁷, I.A. Savin⁸, G. Sbrizzai^{25,26}, P. Schiavon^{25,26}, K. Schmidt^{10,e}, H. Schmieden⁵, K. Schönning^{11,k}, S. Schopferer¹⁰, A. Selyunin⁸, O.Yu. Shevchenko^{8,*}, L. Silva¹³, L. Sinha⁷, S. Sirtl¹⁰, M. Slunecka⁸, F. Sozzi²⁶, A. Srnka⁶, M. Stolarski¹³, M. Sulc¹², H. Suzuki^{34,f}, A. Szabelski³¹, T. Szameitat^{10,e}, P. Sznajder³¹, S. Takekawa^{28,29}, J. ter Wolbeek^{10,e}, S. Tessaro²⁶, F. Tessarotto²⁶, F. Thibaud²², F. Tosello²⁹, V. Tskhay¹⁶, S. Uhl¹⁷, J. Veloso², M. Virius²⁰, T. Weisrock¹⁴, M. Wilfert¹⁴, R. Windmolders⁵, K. Zaremba³³, M. Zavertyaev¹⁶, E. Zemlyanichkina⁸, M. Ziembicki³³ and A. Zink⁹

¹ University of Eastern Piedmont, 15100 Alessandria, Italy

² University of Aveiro, Department of Physics, 3810-193 Aveiro, Portugal

³ Universität Bochum, Institut für Experimentalphysik, 44780 Bochum, Germany^{ls}

⁴ Universität Bonn, Helmholtz-Institut für Strahlen- und Kernphysik, 53115 Bonn, Germany^l

⁵ Universität Bonn, Physikalisches Institut, 53115 Bonn, Germany^l

⁶ Institute of Scientific Instruments, AS CR, 61264 Brno, Czech Republic^m

⁷ Matrivani Institute of Experimental Research & Education, Calcutta-700 030, Indiaⁿ

⁸ Joint Institute for Nuclear Research, 141980 Dubna, Moscow region, Russia^o

⁹ Universität Erlangen–Nürnberg, Physikalisches Institut, 91054 Erlangen, Germany^l

¹⁰ Universität Freiburg, Physikalisches Institut, 79104 Freiburg, Germany^{ls}

¹¹ CERN, 1211 Geneva 23, Switzerland

¹² Technical University in Liberec, 46117 Liberec, Czech Republic^m

¹³ LIP, 1000-149 Lisbon, Portugal^p

¹⁴ Universität Mainz, Institut für Kernphysik, 55099 Mainz, Germany^l

- ¹⁵ University of Miyazaki, Miyazaki 889-2192, Japan^q
- ¹⁶ Lebedev Physical Institute, 119991 Moscow, Russia
- ¹⁷ Technische Universität München, Physik Department, 85748 Garching, Germany^{lr}
- ¹⁸ Nagoya University, 464 Nagoya, Japan^q
- ¹⁹ Charles University in Prague, Faculty of Mathematics and Physics, 18000 Prague, Czech Republic^m
- ²⁰ Czech Technical University in Prague, 16636 Prague, Czech Republic^m
- ²¹ State Scientific Center Institute for High Energy Physics of National Research Center ‘Kurchatov Institute’, 142281 Protvino, Russia
- ²² CEA IRFU/SPhN Saclay, 91191 Gif-sur-Yvette, France^s
- ²³ Academia Sinica, Institute of Physics, Taipei, 11529 Taiwan
- ²⁴ Tel Aviv University, School of Physics and Astronomy, 69978 Tel Aviv, Israel^t
- ²⁵ University of Trieste, Department of Physics, 34127 Trieste, Italy
- ²⁶ Trieste Section of INFN, 34127 Trieste, Italy
- ²⁷ Abdus Salam ICTP, 34151 Trieste, Italy
- ²⁸ University of Turin, Department of Physics, 10125 Turin, Italy
- ²⁹ Torino Section of INFN, 10125 Turin, Italy
- ³⁰ University of Illinois at Urbana-Champaign, Department of Physics, Urbana, IL 61801-3080, U.S.A.
- ³¹ National Centre for Nuclear Research, 00-681 Warsaw, Poland^u
- ³² University of Warsaw, Faculty of Physics, 02-093 Warsaw, Poland^u
- ³³ Warsaw University of Technology, Institute of Radioelectronics, 00-665 Warsaw, Poland^u
- ³⁴ Yamagata University, Yamagata, 992-8510 Japan^q
- ^a Retired from Universität Bielefeld, Fakultät für Physik, 33501 Bielefeld, Germany
- ^b Also at Instituto Superior Técnico, Universidade de Lisboa, Lisbon, Portugal
- ^c Present address: Universität Mainz, Helmholtz-Institut für Strahlen- und Kernphysik, 55099 Mainz, Germany
- ^d Also at Department of Physics, Pusan National University, Busan 609-735, Republic of Korea and at Physics Department, Brookhaven National Laboratory, Upton, NY 11973, U.S.A.
- ^e Supported by the DFG Research Training Group Programme 1102 “Physics at Hadron Accelerators”
- ^f Also at Chubu University, Kasugai, Aichi, 487-8501 Japan^q
- ^g Also at KEK, 1-1 Oho, Tsukuba, Ibaraki, 305-0801 Japan
- ^h Present address: Universität Bonn, Helmholtz-Institut für Strahlen- und Kernphysik, 53115 Bonn, Germany
- ⁱ Also at Moscow Institute of Physics and Technology, Moscow Region, 141700, Russia
- ^j Present address: RWTH Aachen University, III. Physikalisches Institut, 52056 Aachen, Germany
- ^k Present address: Uppsala University, Box 516, SE-75120 Uppsala, Sweden
- ^l Supported by the German Bundesministerium für Bildung und Forschung
- ^m Supported by Czech Republic MEYS Grant LG13031
- ⁿ Supported by SAIL (CSR), Govt. of India
- ^o Supported by CERN-RFBR Grant 12-02-91500
- ^p Supported by the Portuguese FCT - Fundação para a Ciência e Tecnologia, COMPETE and QREN, Grants CERN/FP/109323/2009, CERN/FP/116376/2010 and CERN/FP/123600/2011
- ^q Supported by the MEXT and the JSPS under the Grants No.18002006, No.20540299 and No.18540281; Daiko Foundation and Yamada Foundation
- ^r Supported by the DFG cluster of excellence ‘Origin and Structure of the Universe’ (www.universe-cluster.de)
- ^s Supported by EU FP7 (HadronPhysics3, Grant Agreement number 283286)
- ^t Supported by the Israel Science Foundation, founded by the Israel Academy of Sciences and Humanities

^u Supported by the Polish NCN Grant DEC-2011/01/M/ST2/02350
* Deceased

1 Introduction

The determination of the longitudinal spin structure of the nucleon became one of the important issues in particle physics after the surprising EMC result that the quark contribution to the nucleon spin is very small or even vanishing [1]. The present knowledge on the longitudinal spin structure function of the proton, g_1^p , originates from measurements of the asymmetry A_1^p in polarised lepton nucleon scattering. In all these experiments, longitudinally polarised high-energy leptons were scattered off longitudinally polarised nucleon or nuclear targets. At SLAC and JLab electron beams were used, electron and positron beams at DESY and muon beams at CERN. Details on the performance of these experiments and a collection of their results can be found e.g. in Ref. 2.

In this Letter, we report on new results from the COMPASS experiment at CERN. By measuring A_1^p , we obtain results on g_1^p in the deep inelastic scattering (DIS) region. They cover the range from $1 (\text{GeV}/c)^2$ to $190 (\text{GeV}/c)^2$ in the photon virtuality Q^2 and from 0.0025 to 0.7 in the Bjorken scaling variable x . The new data, which were collected in 2011 at a beam energy of 200 GeV, complement earlier data taken in 2007 at 160 GeV that covered the range $0.004 < x < 0.7$ [3]. In the newly explored low- x region, our results significantly improve the statistical precision of g_1^p and thereby allow us to decrease the low- x extrapolation uncertainty in the determination of first moments.

In the following section, the COMPASS experiment is briefly described. The data selection procedure is presented in Section 3 and the method of asymmetry calculation in Section 4. The results on $A_1^p(x, Q^2)$ and $g_1^p(x, Q^2)$ are given in Section 5. A new next-to-leading order (NLO) QCD fit to the existing nucleon g_1 data in the region $Q^2 > 1 (\text{GeV}/c)^2$ is described in Section 6. Section 7 deals with the determination of first moments of g_1^p and the evaluation of the Bjorken sum rule using COMPASS data only. Conclusions are given in Section 8.

2 Experimental setup

The measurements were performed with the COMPASS setup at the M2 beam line of the CERN SPS. The data presented in this Letter correspond to an integrated luminosity of 0.52 fb^{-1} . A beam of positive muons was used with an intensity of 10^7 s^{-1} in a 10 s long spill every 40 s. The nominal beam momentum was 200 GeV/c with a spread of 5%. The beam was naturally polarised with an average polarisation $P_B = 0.83$, which is known with a precision of 0.04. Momentum and trajectory of each incoming particle were measured in a set of scintillator hodoscopes, scintillating fibre and silicon detectors. The beam was impinging on a solid-state ammonia (NH_3) target that provides longitudinally polarised protons. The three protons in ammonia were polarised up to $|P_T| \approx 0.9$ by dynamic nuclear polarisation with microwaves. For this purpose, the target was placed inside a large-aperture superconducting solenoid with a field of 2.5 T and cooled to 60 mK by a mixture of liquid ^3He and ^4He . The target material was contained in three cylindrical cells with a diameter of 4 cm, which had their axes along the beam line and were separated by a distance of 5 cm. The outer cells with a length of 30 cm were oppositely polarised to the central one, which was 60 cm long. In order to compensate for acceptance differences between the cells, the polarisation was regularly reversed by rotation of the magnetic field direction. In order to guard against unknown systematic effects, once during the data taking period the direction of the polarisation relative to the magnetic field was reversed by exchanging the microwave frequencies applied to the cells. Ten NMR coils surrounding the target material allowed for a measurement of P_T with a precision of 0.032 for both signs of the polarisation. The typical dilution due to unpolarisable material in the target amounts to about 0.15.

The experimental setup allowed for the measurement of scattered muons and produced hadrons. These particles were detected in a two-stage, open forward spectrometer with large acceptance in momentum

and angle. Each spectrometer stage consisted of a dipole magnet surrounded by tracking detectors. Scintillating fibre detectors and pixel GEM detectors in the beam region were supplemented with Micromegas and GEM detectors close to the beam and MWPCs, drift chambers and straw detectors that covered the large outer areas. Scattered muons were identified in sets of drift-tube planes located behind iron and concrete absorbers in the first and second stages. Particle identification with the RICH detector or calorimeters is not used in this measurement. The ‘inclusive triggers’ were based on a combination of hodoscope signals for the scattered muons, while for ‘semi-inclusive’ triggers an energy deposit of hadron tracks in one of the calorimeters was required, optionally in coincidence with an inclusive trigger. A detailed description of the experimental setup can be found in Ref. 4.

3 Data selection

The selected events are required to contain a reconstructed incoming muon, a scattered muon and an interaction vertex. The measured incident muon momentum has to be in the range $185 \text{ GeV}/c < p_B < 215 \text{ GeV}/c$. In order to equalise the beam flux through all target cells, the extrapolated beam track is required to pass all of them. The measured longitudinal position of the vertex allows us to identify the target cell in which the scattering occurred. The radial distance of the vertex from the beam axis is required to be less than 1.9 cm, by which the contribution of unpolarised material is minimised. All physics triggers, inclusive and semi-inclusive ones, are included in this analysis. In order to be attributed to the scattered muon, a track is required to pass more than 30 radiation lengths of material and it has to point to the hodoscopes that have triggered the event. In order to select the region of deep inelastic scattering, only events with photon virtuality $Q^2 > 1 (\text{GeV}/c)^2$ are selected. In addition, the relative muon energy transfer, y , is required to be between 0.1 and 0.9. Here, the lower limit removes events that are difficult to reconstruct, while the upper limit removes the region that is dominated by radiative events. These kinematic constraints lead to the range $0.0025 < x < 0.7$ and to a minimum mass squared of the hadronic final state, W^2 , of $12 (\text{GeV}/c^2)^2$. After all selections, the final sample consists of 77 million events. The selected sample is dominated by inclusive triggers that contribute 84% to the total number of triggers. The semi-inclusive triggers mainly contribute to the high- x region, where they amount to about half of the triggers. In the high- Q^2 region the semi-inclusive triggers dominate.

4 Asymmetry calculation

The asymmetry between the cross sections for antiparallel ($\uparrow\downarrow$) and parallel ($\uparrow\uparrow$) orientations of the longitudinal spins of incoming muon and target proton is written as

$$A_{\text{LL}}^{\text{p}} = \frac{\sigma^{\uparrow\downarrow} - \sigma^{\uparrow\uparrow}}{\sigma^{\uparrow\downarrow} + \sigma^{\uparrow\uparrow}}. \quad (1)$$

This asymmetry is related to the longitudinal and transverse spin asymmetries A_1^{p} and A_2^{p} , respectively, for virtual-photon absorption by the proton:

$$A_{\text{LL}}^{\text{p}} = D(A_1^{\text{p}} + \eta A_2^{\text{p}}). \quad (2)$$

The factors

$$\eta = \frac{\gamma(1-y-\gamma^2 y^2/4 - y^2 m^2/Q^2)}{(1+\gamma^2 y/2)(1-y/2) - y^2 m^2/Q^2} \quad (3)$$

and

$$D = \frac{y((1+\gamma^2 y/2)(2-y) - 2y^2 m^2/Q^2)}{y^2(1-2m^2/Q^2)(1+\gamma^2) + 2(1+R)(1-y-\gamma^2 y^2/4)} \quad (4)$$

depend on the event kinematics, with $\gamma = 2Mx/\sqrt{Q^2}$. The virtual-photon depolarisation factor D depends also on the ratio $R = \sigma_L/\sigma_T$, where σ_L (σ_T) is the cross section for the absorption of a longitudinally (transversely) polarised virtual photon by a proton. The asymmetry A_1^p is defined as

$$A_1^p = \frac{\sigma_{1/2} - \sigma_{3/2}}{\sigma_{1/2} + \sigma_{3/2}}, \quad (5)$$

where $\sigma_{1/2}$ ($\sigma_{3/2}$) is the absorption cross section of a transversely polarised virtual photon by a proton with total spin projection $\frac{1}{2}$ ($\frac{3}{2}$) in the photon direction. Since both η and A_2^p [5] are small in the COMPASS kinematic region, $A_1^p \simeq A_{LL}^p/D$ and the longitudinal spin structure function is given by

$$g_1^p = \frac{F_2^p}{2x(1+R)}A_1^p, \quad (6)$$

where F_2^p denotes the spin-independent structure function of the proton.

The number of events, N_i , collected from each target cell before and after reversal of the target polarisation is related to the spin-independent cross section $\bar{\sigma} = \sigma_{1/2} + \sigma_{3/2}$ and to the asymmetry A_1^p as

$$N_i = a_i \phi_i n_i \bar{\sigma} (1 + P_B P_T f D A_1^p), \quad i = o1, c1, o2, c2. \quad (7)$$

Here, a_i is the acceptance, ϕ_i the incoming muon flux, n_i the number of target nucleons and f the dilution factor, while P_B and P_T were already introduced in Section 2. Events from the outer target cell are summed, thus the four relations of Eq. (7) corresponding to the two sets of target cells (outer, o and central, c) and the two spin orientations (1 and 2) result in a second-order equation in A_1^p for the ratio $(N_{o1}N_{c2})/(N_{c1}N_{o2})$. Fluxes and acceptances cancel in this equation, if the ratio of acceptances for the two sets of cells is the same before and after the magnetic field rotation [6]. In order to minimise the statistical uncertainty, all quantities used in the asymmetry calculation are evaluated event by event with the weight factor [6]

$$w = P_B f D. \quad (8)$$

The polarisation of the incoming muons as a function of the beam momentum is obtained from a parametrisation based on a Monte Carlo simulation of the beam line. The effective dilution factor f is given by the ratio of the total cross section for muons on polarisable protons to the one on all nuclei in the target, whereby their measured composition is taken into account. It is modified by a correction factor that accounts for the dilution due to radiative events on unpolarised protons [7]. The target polarisation is not included in the event weight, because it may change in time and generate false asymmetries. The obtained asymmetries are corrected for spin-dependent radiative effects according to Ref. 8 and for the ^{14}N polarisation as described in Refs. 3, 9. It has been checked that the use of semi-inclusive triggers does not bias the determination of A_1^p .

Systematic uncertainties are calculated taking into account multiplicative and additive contributions to A_1^p . Multiplicative contributions originate from the uncertainties of the target polarisation, the beam polarisation, the dilution factor (mainly due to the uncertainty of R) and the depolarisation factor. When added in quadrature, these uncertainties result in a total uncertainty ΔA_1^{mult} of $0.07A_1^p$. They are shown in Table 1, which also shows the additive contributions. The largest additive contribution to the systematic uncertainty is the one from possible false asymmetries. Its size is estimated with two different approaches. In the first approach, the central target cell is artificially divided into two consecutive 30cm long parts. Combining these two 30cm long targets with the outer ones with the same polarisation, two independent false asymmetries are formed. Both are found to be consistent with zero. In order to check for time-dependent effects, in the second approach the data sample is divided into sub-samples each consisting of periods of stable data taking with both field directions for each target cell. The results for

Table 1: Contributions to the systematic uncertainty on A_1^P with multiplicative (top) and additive (bottom) components.

Beam polarisation	$\Delta P_B/P_B$	5%
Target polarisation	$\Delta P_T/P_T$	3.5%
Depolarisation factor	$\Delta D(R)/D(R)$	2.0 – 3.0%
Dilution factor	$\Delta f/f$	2%
Total	ΔA_1^{mult}	$\simeq 0.07A_1$
False asymmetry	A_{false}	$< 0.84 \cdot \sigma_{\text{stat}}$
Transverse asymmetry	$\eta \cdot A_2$	$< 10^{-2}$
Radiative corrections	A_1^{RC}	$10^{-4} - 10^{-3}$

A_1^P obtained from these sub-samples are compared by using the method of “pulls” [10]. No significant broadening of pull distributions is observed. These pulls are used to set an upper limit on the systematic uncertainty due to false asymmetries A_1^{false} . Depending on the x -bin, values between $0.4 \cdot \sigma_{\text{stat}}$ and $0.84 \cdot \sigma_{\text{stat}}$ are obtained. Further additive corrections originate from neglecting A_2 and from the uncertainty in the correction A_1^{RC} to the asymmetry A_1 , which is due to spin-dependent radiative effects.

5 Results on A_1^P and g_1^P

The data are analysed in terms of A_1 and g_1 as a function of x and Q^2 . The x dependence of A_1^P averaged over Q^2 in each x bin is shown in Fig. 1 together with the previous COMPASS results obtained at 160 GeV [3] and with results from other experiments [1, 11–14] including those by SMC at 190 GeV [15]. The bands at the bottom represent the systematic uncertainties of the COMPASS results as discussed in Section 4. The new data improve the statistical precision at least by a factor of two in the low- x region, which is covered by the SMC and COMPASS measurements only. The good agreement between all experimental results reflects the weak Q^2 dependence of A_1^P . This is also illustrated in Fig. 2, which shows A_1^P as a function of Q^2 in sixteen intervals of x for the COMPASS data sets at 160 GeV and 200 GeV. In none of the x bins, a significant Q^2 dependence is observed. The numerical values of $A_1^P(x, Q^2)$ obtained at 200 GeV are given in the Appendix.

The longitudinal spin structure function g_1^P is calculated from A_1^P using Eq. (6), the F_2^P parametrisation from Ref. 15 and the ratio R from Ref. 16. The new results are shown in Fig. 3 at the measured values of Q^2 in comparison with the previous COMPASS results obtained at 160 GeV and with SMC results at 190 GeV. Compared to the SMC experiment, the present systematic uncertainties are larger due to a more realistic estimate of false asymmetries, which is based on real events.

The world data on g_1^P as a function of Q^2 for various x are shown in Fig. 4. The data cover about two decades in x and in Q^2 for most of the x range, except for $x < 0.02$, where the Q^2 range is much more limited. The new data improve the kinematic coverage in the region of high Q^2 and low x values, which gives a better lever arm for the determination of quark and gluon polarisations from the DGLAP evolution equations. In addition, the extension of measurements to lower values of x is important to better constrain the value of the first moment of g_1^P .

6 NLO QCD fit of g_1 world data

We performed a new NLO QCD fit of the spin-dependent structure function g_1 in the DIS region, $Q^2 > 1 (\text{GeV}/c)^2$, considering all available proton, deuteron and ^3He data. The fit is performed in

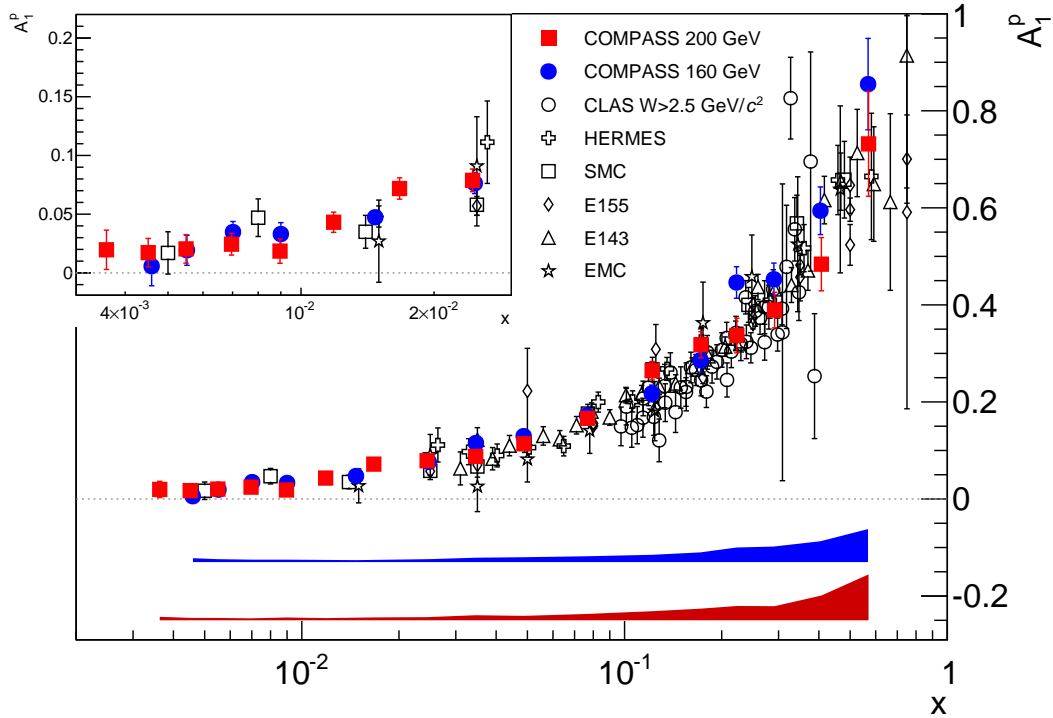


Figure 1: The asymmetry A_1^p as a function of x at the measured values of Q^2 as obtained from the COMPASS data at 200 GeV. The new data are compared to the COMPASS results obtained at 160 GeV [3] and to the other world data (EMC [1], CLAS [11], HERMES [12], E143 [13], E155 [14], SMC [15]). The bands at the bottom indicate the systematic uncertainties of the COMPASS data at 160 GeV (upper band) and 200 GeV (lower band).

the $\overline{\text{MS}}$ renormalisation and factorisation scheme. For the fit, the same program is used as in Ref. 17, which was derived from program 2 in Ref. 15. The region $W^2 < 10 \text{ (GeV}/c^2)^2$ is excluded as it was in recent analyses [18]. Note that the impact of higher-twist effects when using a smaller W^2 cut is considered in Ref. 19. The total number of data points used in the fit is 495 (see Table 2), the number of COMPASS data points is 138.

The neutron structure function g_1^n is extracted from the ^3He data, while the nucleon structure function g_1^N is obtained as

$$g_1^N(x, Q^2) = \frac{1}{1 - 1.5 \omega_D} g_1^d(x, Q^2), \quad (9)$$

where ω_D is a correction for the D-wave state in the deuteron, $\omega_D = 0.05 \pm 0.01$ [24], and the deuteron structure function g_1^d is given per nucleon. The quark singlet distribution $\Delta q^S(x)$, the quark non-singlet distributions $\Delta q_3(x)$ and $\Delta q_8(x)$, as well as the gluon helicity distribution $\Delta g(x)$, which appear in the NLO expressions for g_1^p , g_1^n and g_1^N (see e.g. Ref. 15), are parametrised at a reference scale Q_0^2 as follows:

$$\Delta f_k(x) = \eta_k \frac{x^{\alpha_k} (1-x)^{\beta_k} (1 + \gamma_k x)}{\int_0^1 x^{\alpha_k} (1-x)^{\beta_k} (1 + \gamma_k x) dx}. \quad (10)$$

Here, $\Delta f_k(x)$ ($k = 1 \dots 4$) represents $\Delta q^S(x)$, $\Delta q_3(x)$, $\Delta q_8(x)$ and $\Delta g(x)$ and η_k is the first moment of $\Delta f_k(x)$ at the reference scale. The moments of Δq_3 and Δq_8 are fixed at any scale by the baryon decay constants (F+D) and (3F-D), respectively, assuming $\text{SU}(2)_f$ and $\text{SU}(3)_f$ flavour symmetries. The impact of releasing these conditions is investigated and included in the systematic uncertainty. The coefficients γ_k are fixed to zero for the two non-singlet distributions. The exponent β_g , which is not well determined from the data, is fixed to 3.0225 [25] and the uncertainty from the introduced bias is included in the final

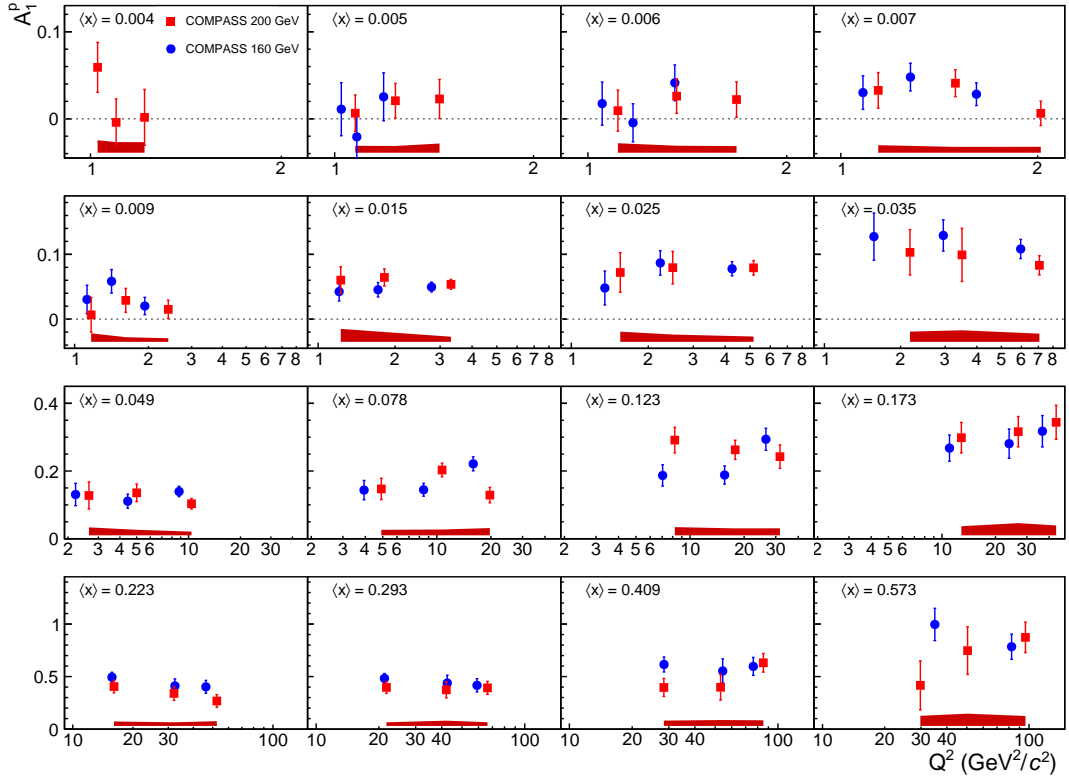


Figure 2: The asymmetry A_1^P as a function of Q^2 in bins of x obtained from the 200 GeV (red squares) and 160 GeV (blue circles) COMPASS data. The band at the bottom indicates the systematic uncertainty for the 200 GeV data.

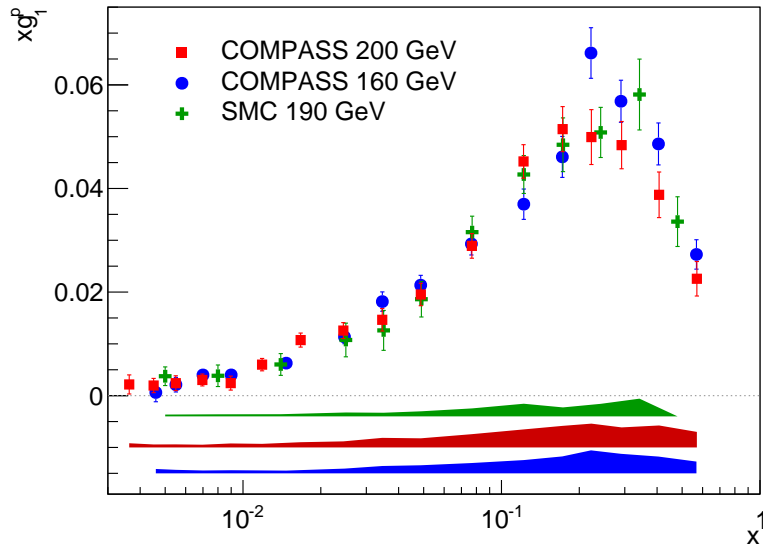


Figure 3: The spin-dependent structure function xg_1^P at the measured values of Q^2 as a function of x . The COMPASS data at 200 GeV (red squares) are compared to the results at 160 GeV (blue circles) and to the SMC results at 190 GeV (green crosses) for $Q^2 > 1$ (GeV/c^2)². The bands from top to bottom indicate the systematic uncertainties for SMC 190 GeV, COMPASS 200 GeV and COMPASS 160 GeV.

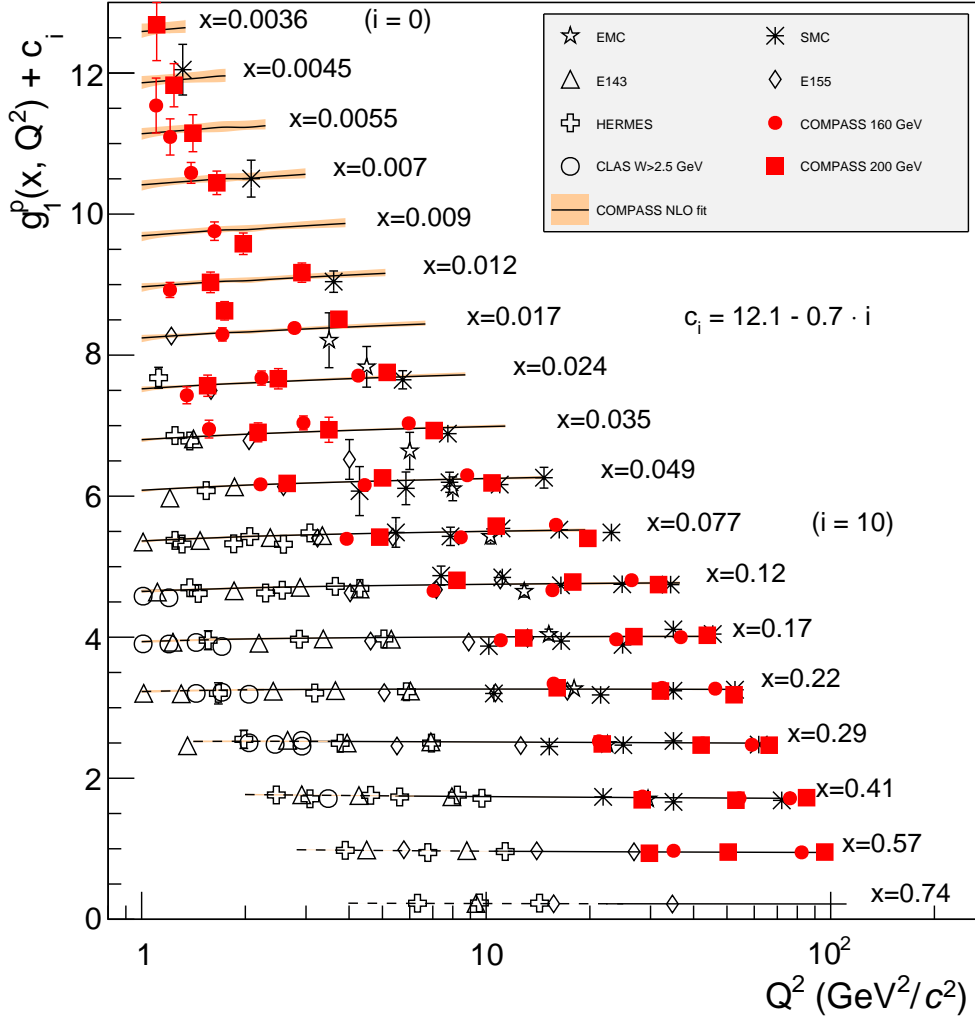


Figure 4: World data on the spin-dependent structure function g_1^p as a function of Q^2 for various values of x with all COMPASS data in red (full circles: 160 GeV, full squares: 200 GeV). The lines represent the Q^2 dependence for each value of x , as determined from a NLO QCD fit (see Section 6). The dashed ranges represent the region with $W^2 < 10$ $(\text{GeV}/c^2)^2$.

uncertainty. This leaves 11 free parameters in the fitted parton distributions. The expression for χ^2 of the fit consists of three terms,

$$\chi^2 = \sum_{n=1}^{N_{\text{exp}}} \left[\sum_{i=1}^{N_n^{\text{data}}} \left(\frac{g_1^{\text{fit}} - \mathcal{N}_n g_{1,i}^{\text{data}}}{\mathcal{N}_n \sigma_i} \right)^2 + \left(\frac{1 - \mathcal{N}_n}{\delta \mathcal{N}_n} \right)^2 \right] + \chi_{\text{positivity}}^2. \quad (11)$$

Only statistical uncertainties of the data are taken into account in σ_i . The normalisation factors \mathcal{N}_n of each data set n are allowed to vary taking into account the normalisation uncertainties $\delta \mathcal{N}_n$. If the latter are unavailable, they are estimated as quadratic sums of the uncertainties of the beam and target polarisations. The fitted normalisations are found to be consistent with unity, except for the E155 proton data where the normalisation is higher, albeit compatible with the value quoted in Ref. 14.

In order to keep the parameters within their physical ranges, the polarised PDFs are calculated at every iteration of the fit and required to satisfy the positivity conditions $|\Delta q(x) + \Delta \bar{q}(x)| \leq q(x) + \bar{q}(x)$

and $|\Delta g(x)| \leq g(x)$ at $Q^2 = 1 \text{ (GeV}/c)^2$, which is accomplished by the $\chi_{\text{positivity}}^2$ term in Eq. (11). This procedure leads to asymmetric values of the parameter uncertainties when the fitted value is close to the allowed limit. The unpolarised PDFs and the corresponding value of the strong coupling constant $\alpha_s(Q^2)$ are taken from the MSTW parametrisation [25]. The impact of the choice of PDFs is evaluated by using the MRST distributions [26] for comparison.

In order to investigate the sensitivity of the parametrisation of the polarised PDFs to the functional forms, the fit is performed for several sets of functional shapes. These shapes do or do not include the γ_S and γ_g parameters of Eq. (10) and are defined at reference scales ranging from $1 \text{ (GeV}/c)^2$ to $63 \text{ (GeV}/c)^2$. It is observed [27] that mainly two sets of functional shapes are needed to span almost entirely the range of the possible $\Delta q^S(x)$ and $\Delta g(x)$ distributions allowed by the data. These two sets of functional forms yield two extreme solutions for $\Delta g(x)$. For $\gamma_g = \gamma_S = 0$ ($\gamma_g = 0$ and $\gamma_S \neq 0$) a negative (positive) solution for $\Delta g(x)$ is obtained. Both solutions are parametrised at $Q_0^2 = 1 \text{ (GeV}/c)^2$ and lead to similar values of the reduced χ^2 of the fits of about 1.05/d.o.f. Changes in the fit result that originate from using other (converging) functional forms are included in the systematic uncertainty.

The obtained distributions are presented in Fig. 5. The dark error bands seen in this figure stem from generating several sets of g_1 pseudo-data, which are obtained by randomising the measured g_1 values using their statistical uncertainties according to a normal distribution. This corresponds to a one-standard-deviation accuracy of the extracted parton distributions. A thorough analysis of systematic uncertainties of the fitting procedure is performed. The most important source is the freedom in the choice of the functional forms for $\Delta q^S(x)$ and $\Delta g(x)$. Further uncertainties arise from the uncertainty in the value of $\alpha_s(Q^2)$ and from effects of $SU(2)_f$ and $SU(3)_f$ symmetry breaking. The systematic uncertainties are represented by the light bands overlaying the dark ones in Fig. 5. For both sets of functional forms discussed above, $\Delta s(x)$ stays negative. It is different from zero for $x \gtrsim 0.001$ as are $\Delta d(x)$ and $\Delta u(x)$. The singlet distribution $\Delta q^S(x)$ is compatible with zero for $x \lesssim 0.07$.

The inclusion of systematic uncertainties in the fit leads to much larger spreads in the first moments as compared to those obtained by only propagating statistical uncertainties (see Table 3). In this table, $\Delta\Sigma$ denotes the first moment of the singlet distribution. Note that the first moments of $\Delta u + \Delta\bar{u}$, $\Delta d + \Delta\bar{d}$ and $\Delta s + \Delta\bar{s}$ are not independent, since the first moments of the non-singlet distributions are fixed by the decay constants F and D at every value of Q^2 . The large uncertainty in $\Delta g(x)$, which is mainly due to the freedom in the choice of its functional form, does however not allow to determine the first moment of $\Delta g(x)$ from the available inclusive data only.

The fitted g_1^p and g_1^d distributions at $Q^2 = 3 \text{ (GeV}/c)^2$ are shown in Fig. 6 together with the data evolved to the same scale. The two curves correspond to the two extreme functional forms discussed above, which lead to either a positive or a negative $\Delta g(x)$. The dark bands represent the statistical uncertainties associated with each curve and the light bands represent the total systematic and statistical uncertainties added in quadrature. The values for g_1^p are positive in the whole measured region down to $x = 0.0025$, while g_1^d is consistent with zero at low x .

7 First moments of g_1 from COMPASS data and Bjorken Sum Rule

The new data on g_1^p together with the new QCD fit allow a more precise determination of the first moments $\Gamma_1(Q^2) = \int_0^1 g_1(x, Q^2) dx$ of the proton, neutron and non-singlet spin structure functions using COMPASS data only. The latter one is defined as

$$g_1^{\text{NS}}(x, Q^2) = g_1^p(x, Q^2) - g_1^n(x, Q^2) = 2[g_1^p(x, Q^2) - g_1^N(x, Q^2)]. \quad (12)$$

Table 2: List of experimental data sets used in this analysis. For each set the number of points, the χ^2 contribution and the fitted normalisation factor is given for the two functional shapes discussed in the text, which lead to either a positive or a negative function $\Delta g(x)$.

Experiment	Function extracted	Number of points	χ^2		Normalisation	
			$\Delta g(x) > 0$	$\Delta g(x) < 0$	$\Delta g(x) > 0$	$\Delta g(x) < 0$
EMC [1]	A_1^p	10	5.2	4.7	1.03 ± 0.07	1.02 ± 0.07
E142 [20]	A_1^n	6	1.1	1.1	1.01 ± 0.07	0.99 ± 0.07
E143 [13]	g_1^d/F_1^d	54	61.4	59.0	0.99 ± 0.04	1.01 ± 0.04
E143 [13]	g_1^p/F_1^p	54	47.4	49.1	1.05 ± 0.02	1.08 ± 0.02
E154 [21]	g_1^d/F_1^d	11	5.9	7.4	1.06 ± 0.04	1.07 ± 0.04
E155 [22]	A_1^n	22	18.8	18.0	1.00 ± 0.04	1.00 ± 0.04
E155 [14]	g_1^d/F_1^d	21	50.0	49.7	1.16 ± 0.02	1.16 ± 0.02
SMC [15]	g_1^p/F_1^p	59	55.4	55.4	1.02 ± 0.03	1.01 ± 0.03
SMC [15]	A_1^p	65	59.3	61.5	1.00 ± 0.04	1.00 ± 0.04
HERMES [12]	A_1^d	24	28.1	27.0	0.98 ± 0.04	1.01 ± 0.04
HERMES [12]	A_1^p	24	14.0	16.2	1.08 ± 0.03	1.10 ± 0.03
HERMES [23]	A_1^n	7	1.6	1.2	1.01 ± 0.07	1.00 ± 0.07
COMPASS 160 GeV [17]	g_1^d	43	33.1	37.7	0.97 ± 0.05	0.95 ± 0.05
COMPASS 160 GeV [3]	g_1^p	44	50.8	49.1	1.00 ± 0.03	0.99 ± 0.03
COMPASS 200 GeV (this work)	A_1^p	51	43.6	43.2	1.03 ± 0.03	1.02 ± 0.03

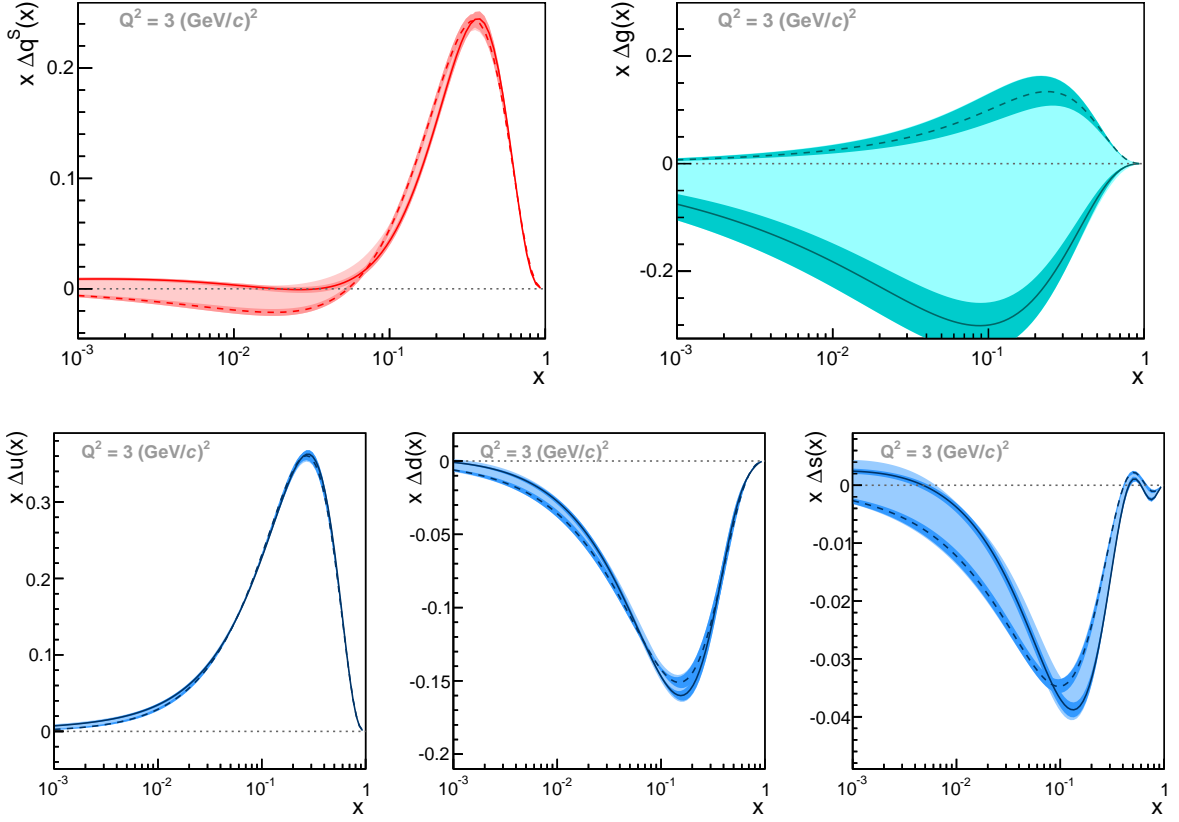


Figure 5: Results of the QCD fits to g_1 world data at $Q^2 = 3 (\text{GeV}/c)^2$ for the two sets of functional shapes as discussed in the text. Top: singlet $x\Delta q^S(x)$ and gluon distribution $x\Delta g(x)$. Bottom: distributions of $x[\Delta q(x) + \Delta \bar{q}(x)]$ for different flavours (u , d and s). Continuous lines correspond to the fit with $\gamma_S = 0$, long dashed lines to the one with $\gamma_S \neq 0$. The dark bands represent the statistical uncertainties, only. The light bands, which overlay the dark ones, represent the systematic uncertainties.

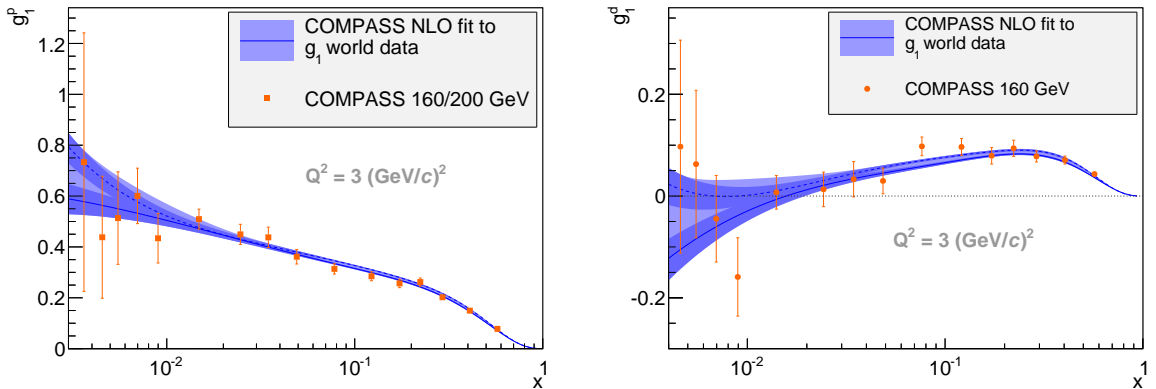


Figure 6: Results of the QCD fits to g_1^p (left) and g_1^d (right) world data at $Q^2 = 3 (\text{GeV}/c)^2$ as functions of x . The curves correspond to the two sets of functional shapes as discussed in the text. The dark bands represent the statistical uncertainties associated with each curve and the light bands, which overlay the dark ones, represent the systematic uncertainties.

Table 3: Value ranges of first moments of quark distributions, as obtained from the QCD fit when taking into account both statistical and systematic uncertainties, as detailed in the text.

First moment	Value range at $Q^2 = 3 (\text{GeV}/c)^2$
$\Delta\Sigma$	[0.26 , 0.36]
$\Delta u + \Delta\bar{u}$	[0.82 , 0.85]
$\Delta d + \Delta\bar{d}$	[-0.45 , -0.42]
$\Delta s + \Delta\bar{s}$	[-0.11 , -0.08]

Table 4: Contribution to the first moments of g_1 at $Q^2 = 3 (\text{GeV}/c)^2$ with statistical uncertainties from the COMPASS data. Limits in parentheses are applied for the calculation of Γ_1^N . The uncertainties of the extrapolations are negligible.

x range	Γ_1^p	Γ_1^N
0 – 0.0025 (0.004)	0.002	0.000
0.0025 (0.004) – 0.7	0.134 ± 0.003	0.047 ± 0.003
0.7 – 1.0	0.003	0.001

Table 5: First moments of g_1 at $Q^2 = 3 (\text{GeV}/c)^2$ using COMPASS data only.

	Γ_1	$\delta\Gamma_1^{\text{stat}}$	$\delta\Gamma_1^{\text{syst}}$	$\delta\Gamma_1^{\text{evol}}$
Proton	0.139	± 0.003	± 0.009	± 0.005
Nucleon	0.049	± 0.003	± 0.004	± 0.004
Neutron	-0.041	± 0.006	± 0.011	± 0.005

The integral $\Gamma_1^{\text{NS}}(Q^2)$ at a given value of Q^2 is connected to the ratio g_A/g_V of the axial and vector coupling constants via the fundamental Bjorken sum rule

$$\Gamma_1^{\text{NS}}(Q^2) = \int_0^1 g_1^{\text{NS}}(x, Q^2) dx = \frac{1}{6} \left| \frac{g_A}{g_V} \right| C_1^{\text{NS}}(Q^2), \quad (13)$$

where $C_1^{\text{NS}}(Q^2)$ is the non-singlet coefficient function that is known [28] up to the third order in $\alpha_s(Q^2)$ in perturbative QCD.

Due to small differences in the kinematics of the data sets, all points of the three COMPASS g_1 data sets (Table 2) are evolved to the Q^2 value of the 160 GeV proton data. A weighted average of the 160 GeV and 200 GeV proton data is performed and the points at different values of Q^2 and the same value of x are merged.

For the determination of Γ_1^p and Γ_1^d , the values of g_1^p and g_1^d are evolved to $Q^2 = 3 (\text{GeV}/c)^2$ and the integrals are calculated in the measured ranges of x . In order to obtain the full moments, the QCD fit is used to evaluate the extrapolation to $x = 1$ and $x = 0$ (see Table 4). The moment Γ_1^n is calculated using $g_1^n = 2g_1^N - g_1^p$. The systematic uncertainties of the moments include the uncertainties of P_B , P_T , f and D . In addition, the uncertainties from the QCD evolution and those from the extrapolation are obtained using the uncertainties given in Section 6. The full moments are given in Table 5. Note that also Γ_1^N is updated compared to Ref. [17] using the new QCD fit.

For the evaluation of the Bjorken sum rule, the procedure is slightly modified. Before evolving from the measured Q^2 to $Q^2 = 3 (\text{GeV}/c)^2$, g_1^{NS} is calculated from the proton and deuteron g_1 data. Since there is no measured COMPASS value of g_1^d corresponding to the new g_1^p point at $x = 0.0036$, the value of g_1^d from the NLO QCD fit is used in this case. The fit of g_1^{NS} is performed with the same program as discussed in the previous section but fitting only the non-singlet distribution $\Delta q_3(x, Q^2)$. The parameters of this fit are given in Table 6 and a comparison of the fitted distribution with the data points is shown in Fig. 7. The error band is obtained with the same method as described in the previous section.

Table 6: Results of the fit of $\Delta q_3(x)$ at $Q_0^2 = 1 (\text{GeV}/c)^2$.

Param.	Value
η_3	1.24 ± 0.06
α_3	-0.11 ± 0.08
β_3	$2.2 \begin{smallmatrix} + \\ - \end{smallmatrix} \begin{smallmatrix} 0.5 \\ 0.4 \end{smallmatrix}$
χ^2/NDF	$7.9/13$

Table 7: First moment Γ_1^{NS} at $Q^2 = 3 (\text{GeV}/c)^2$ from the COMPASS data with statistical uncertainties. Contributions from the unmeasured regions are estimated from the NLO fit to g_1^{NS} . The uncertainty is determined using the error band shown in Fig. 7.

x range	Γ_1^{NS}
0 – 0.0025	0.006 ± 0.001
0.0025 – 0.7	0.170 ± 0.008
0.7 – 1.0	0.005 ± 0.002
0 – 1	0.181 ± 0.008

The integral of g_1^{NS} in the measured range of $0.0025 < x < 0.7$ is calculated using the data points. The contribution from the unmeasured region is extracted again from the fit. The various contributions are listed in Table 7 and the dependence of Γ_1^{NS} on the lower limit of the integral is shown in Fig. 8. The contribution of the measured x range to the integral corresponds to 93.8% of the full first moment, while the extrapolation to 0 and 1 amounts to 3.6% and 2.6%, respectively. Compared to the previous result [3], the contribution of the extrapolation to $x = 0$ is now by about one third smaller than before due to the larger x range of the present data. The value of the integral for the full x range is

$$\Gamma_1^{\text{NS}} = 0.181 \pm 0.008 (\text{stat.}) \pm 0.014 (\text{syst.}) . \quad (14)$$

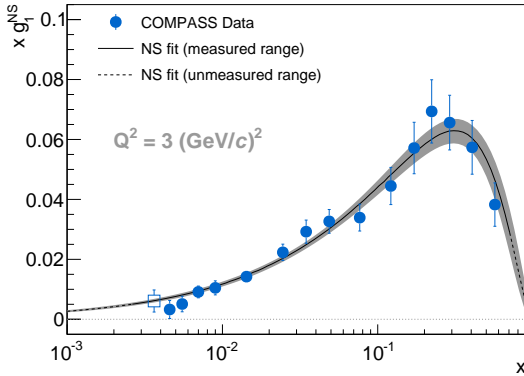


Figure 7: Values of $xg_1^{\text{NS}}(x)$ at $Q^2 = 3 (\text{GeV}/c)^2$ compared to the non-singlet NLO QCD fit using COMPASS data only. The errors bars are statistical. The open square at lowest x is obtained with g_1^{d} taken from the NLO QCD fit.

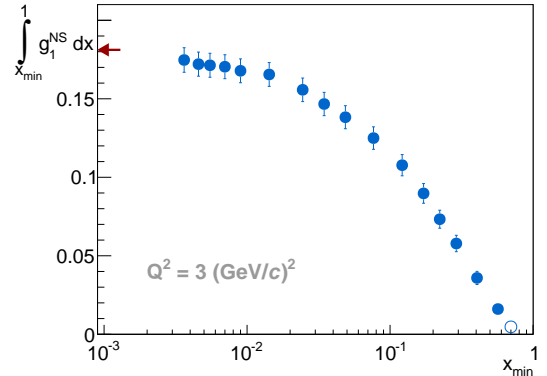


Figure 8: Values of $\int_{x_{\text{min}}}^1 g_1^{\text{NS}} dx$ as a function of x_{min} . The open circle at $x = 0.7$ is obtained from the fit. The arrow on the left side shows the value for the full range, $0 \leq x \leq 1$.

The uncertainty of Γ_1^{NS} is dominated by the systematic uncertainties. The largest contribution stems from the uncertainty of the beam polarisation (5%); other contributions originate from uncertainties in the combined proton data, i.e. those of target polarisation, dilution factor and depolarisation factor. The uncertainties in the deuteron data have a smaller impact as the first moment of g_1^{d} is smaller than that of the proton. The uncertainty due to the evolution to a common Q^2 is found to be negligible when varying Q_0^2 between $1 (\text{GeV}/c)^2$ and $10 (\text{GeV}/c)^2$. The overall result agrees well with our earlier result $\Gamma_1^{\text{NS}} = 0.190 \pm 0.009 \pm 0.015$ in [3].

The result for Γ_1^{NS} is used to evaluate the Bjorken sum rule with Eq. (13). Using the coefficient function $C_1^{\text{NS}}(Q^2)$ at NLO and $\alpha_s = 0.337$ at $Q^2 = 3 (\text{GeV}/c)^2$, one obtains

$$|g_A/g_V| = 1.22 \pm 0.05 \text{ (stat.)} \pm 0.10 \text{ (syst.)}. \quad (15)$$

The comparison of the value of $|g_A/g_V|$ from the present analysis and the one obtained from neutron β decay, $|g_A/g_V| = 1.2701 \pm 0.002$ [29], provides a validation of the Bjorken sum rule with an accuracy of 9%. Note that the contribution of Δg cancels in Eq. (12) and hence does not enter the Bjorken sum. Higher-order perturbative corrections are expected to increase slightly the result. By using the coefficient function C_1^{NS} at NNLO instead of NLO, $|g_A/g_V|$ is found to be 1.25, closer to values stemming from the neutron weak decay.

8 Conclusions

The COMPASS Collaboration performed new measurements of the longitudinal double spin asymmetry $A_1^p(x, Q^2)$ and the longitudinal spin structure function $g_1^p(x, Q^2)$ of the proton in the range $0.0025 < x < 0.7$ and in the DIS region, $1 < Q^2 < 190 \text{ (GeV}/c)^2$, thus extending the previously covered kinematic range [3] towards large values of Q^2 and small values of x . The new data improve the statistical precision of $g_1^p(x)$ by about a factor of two for $x \lesssim 0.02$.

The world data for g_1^p , g_1^d and g_1^n were used to perform a NLO QCD analysis, including a detailed investigation of systematic effects. This analysis thus updates and supersedes the previous COMPASS QCD analysis [17]. It was found that the contribution of quarks to the nucleon spin, $\Delta\Sigma$, lies in the interval 0.26 and 0.36 at $Q^2 = 3 \text{ (GeV}/c)^2$, where the interval limits reflect mainly the large uncertainty in the determination of the gluon contribution.

When combined with the previously published results on the deuteron [17], the new g_1^p data provide a new determination of the non-singlet spin structure function g_1^{NS} and a new evaluation of the Bjorken sum rule, which is validated to an accuracy of about 9 %.

Acknowledgements

We gratefully acknowledge the support of the CERN management and staff and the skill and effort of the technicians of our collaborating institutes. This work was made possible by the financial support of our funding agencies.

A Asymmetry Results

References

- [1] EMC, J. Ashman, et al., Phys. Lett. B 206 (1988) 364; Nucl. Phys. B 328 (1989) 1.
- [2] C.A. Aidala, S.D. Bass, D. Hasch and G.K. Mallot, Rev. Mod. Phys. 85 (2013) 655.
- [3] COMPASS Collaboration, M.G. Alekseev, et al., Phys. Lett. B 690 (2010) 466.
- [4] COMPASS Collaboration, P. Abbon, et al., Nucl. Instr. Meth. A 577 (2007) 455.
- [5] E155 Collaboration, P.L. Anthony, et al., Phys. Lett. B 553 (2003) 18.
- [6] SMC, D. Adams, et al., Phys. Rev. D 56 (1997) 5330.
- [7] A.A. Akhundov, et al., Fortsch. Phys. 44 (1996) 373.
- [8] I.V. Akushevich and N.M. Shumeiko, J. Phys. G 20 (1994) 513.

Table A.1: Values of A_1^P and g_1^P as a function of x at the measured values of Q^2 . The first uncertainty is statistical, the second one systematic.

x range	$\langle x \rangle$	Q^2 ((GeV/c) ²)	A_1^P	g_1^P
0.0025 – 0.004	0.0035	1.03	$0.059 \pm 0.029 \pm 0.014$	$1.79 \pm 0.87 \pm 0.45$
	0.0036	1.10	$-0.004 \pm 0.027 \pm 0.012$	$-0.12 \pm 0.81 \pm 0.37$
	0.0038	1.22	$0.002 \pm 0.032 \pm 0.012$	$0.05 \pm 0.98 \pm 0.37$
0.004 – 0.005	0.0044	1.07	$0.006 \pm 0.021 \pm 0.008$	$0.15 \pm 0.50 \pm 0.19$
	0.0045	1.24	$0.021 \pm 0.020 \pm 0.008$	$0.53 \pm 0.51 \pm 0.20$
	0.0046	1.44	$0.023 \pm 0.022 \pm 0.011$	$0.60 \pm 0.59 \pm 0.28$
0.005 – 0.006	0.0055	1.11	$0.009 \pm 0.024 \pm 0.011$	$0.18 \pm 0.46 \pm 0.21$
	0.0055	1.36	$0.026 \pm 0.020 \pm 0.008$	$0.56 \pm 0.42 \pm 0.17$
	0.0056	1.68	$0.022 \pm 0.020 \pm 0.008$	$0.51 \pm 0.47 \pm 0.18$
0.006 – 0.008	0.0069	1.14	$0.033 \pm 0.020 \pm 0.009$	$0.50 \pm 0.32 \pm 0.14$
	0.0069	1.50	$0.041 \pm 0.015 \pm 0.007$	$0.71 \pm 0.27 \pm 0.12$
	0.0071	2.02	$0.006 \pm 0.014 \pm 0.007$	$0.12 \pm 0.27 \pm 0.13$
0.008 – 0.010	0.0089	1.17	$0.007 \pm 0.027 \pm 0.013$	$0.08 \pm 0.32 \pm 0.16$
	0.0089	1.62	$0.029 \pm 0.018 \pm 0.007$	$0.40 \pm 0.25 \pm 0.10$
	0.0090	2.41	$0.015 \pm 0.014 \pm 0.006$	$0.24 \pm 0.23 \pm 0.09$
0.010 – 0.014	0.0116	1.21	$0.044 \pm 0.026 \pm 0.013$	$0.41 \pm 0.24 \pm 0.12$
	0.0117	1.75	$0.040 \pm 0.017 \pm 0.011$	$0.42 \pm 0.18 \pm 0.11$
	0.0120	2.92	$0.044 \pm 0.011 \pm 0.005$	$0.56 \pm 0.14 \pm 0.07$
0.014 – 0.020	0.0164	1.26	$0.087 \pm 0.034 \pm 0.015$	$0.58 \pm 0.22 \pm 0.11$
	0.0165	1.92	$0.100 \pm 0.020 \pm 0.011$	$0.77 \pm 0.16 \pm 0.09$
	0.0168	3.74	$0.063 \pm 0.011 \pm 0.006$	$0.60 \pm 0.10 \pm 0.06$
0.020 – 0.030	0.0239	1.55	$0.072 \pm 0.030 \pm 0.016$	$0.36 \pm 0.15 \pm 0.08$
	0.0240	2.49	$0.079 \pm 0.025 \pm 0.011$	$0.45 \pm 0.14 \pm 0.07$
	0.0246	5.16	$0.079 \pm 0.011 \pm 0.008$	$0.545 \pm 0.077 \pm 0.061$
0.030 – 0.040	0.0341	2.18	$0.103 \pm 0.035 \pm 0.016$	$0.39 \pm 0.13 \pm 0.06$
	0.0343	3.50	$0.099 \pm 0.041 \pm 0.018$	$0.43 \pm 0.18 \pm 0.08$
	0.0347	7.07	$0.083 \pm 0.015 \pm 0.013$	$0.421 \pm 0.075 \pm 0.066$
0.040 – 0.060	0.0473	2.65	$0.128 \pm 0.040 \pm 0.023$	$0.37 \pm 0.12 \pm 0.07$
	0.0480	5.00	$0.136 \pm 0.026 \pm 0.016$	$0.449 \pm 0.086 \pm 0.057$
	0.0492	10.4	$0.103 \pm 0.015 \pm 0.011$	$0.378 \pm 0.056 \pm 0.043$
0.060 – 0.100	0.0740	4.91	$0.147 \pm 0.031 \pm 0.016$	$0.308 \pm 0.066 \pm 0.036$
	0.0754	10.7	$0.203 \pm 0.020 \pm 0.017$	$0.465 \pm 0.047 \pm 0.043$
	0.0800	19.7	$0.129 \pm 0.023 \pm 0.021$	$0.292 \pm 0.052 \pm 0.050$
0.100 – 0.150	0.119	8.23	$0.291 \pm 0.038 \pm 0.024$	$0.397 \pm 0.051 \pm 0.035$
	0.121	17.8	$0.263 \pm 0.028 \pm 0.021$	$0.372 \pm 0.040 \pm 0.031$
	0.125	31.7	$0.242 \pm 0.034 \pm 0.021$	$0.337 \pm 0.048 \pm 0.030$
0.150 – 0.200	0.171	12.9	$0.299 \pm 0.045 \pm 0.027$	$0.279 \pm 0.042 \pm 0.026$
	0.172	26.9	$0.316 \pm 0.045 \pm 0.036$	$0.298 \pm 0.042 \pm 0.035$
	0.175	43.8	$0.344 \pm 0.050 \pm 0.029$	$0.318 \pm 0.046 \pm 0.028$
0.200 – 0.250	0.222	16.1	$0.405 \pm 0.060 \pm 0.043$	$0.273 \pm 0.040 \pm 0.030$
	0.222	32.1	$0.340 \pm 0.066 \pm 0.035$	$0.227 \pm 0.044 \pm 0.024$
	0.224	52.4	$0.268 \pm 0.060 \pm 0.045$	$0.174 \pm 0.039 \pm 0.030$
0.250 – 0.350	0.289	21.7	$0.397 \pm 0.057 \pm 0.035$	$0.176 \pm 0.025 \pm 0.016$
	0.290	42.1	$0.374 \pm 0.077 \pm 0.050$	$0.160 \pm 0.033 \pm 0.022$
	0.296	66.3	$0.392 \pm 0.062 \pm 0.035$	$0.159 \pm 0.025 \pm 0.015$
0.350 – 0.500	0.403	28.4	$0.396 \pm 0.086 \pm 0.051$	$0.085 \pm 0.018 \pm 0.011$
	0.405	53.1	$0.40 \pm 0.12 \pm 0.06$	$0.079 \pm 0.024 \pm 0.011$
	0.413	85.1	$0.631 \pm 0.088 \pm 0.054$	$0.114 \pm 0.016 \pm 0.010$
0.500 – 0.700	0.561	29.8	$0.42 \pm 0.23 \pm 0.10$	$0.028 \pm 0.016 \pm 0.006$
	0.567	50.4	$0.75 \pm 0.23 \pm 0.12$	$0.044 \pm 0.013 \pm 0.007$
	0.575	96.1	$0.87 \pm 0.15 \pm 0.09$	$0.0429 \pm 0.0071 \pm 0.0048$

- [9] O.A. Rondon, Phys. Rev. C 60 (1999) 035201.
- [10] COMPASS Collaboration, E.S. Ageev, et al., Nucl. Phys. B 765 (2007) 31.
- [11] CLAS Collaboration, K. V. Dharmawardane, et al., Phys. Lett. B 641 (2006) 11.
- [12] HERMES Collaboration, A. Airapetian, et al., Phys. Rev. D 75 (2007) 012007.
- [13] E143 Collaboration, K. Abe, et al., Phys. Rev. D 58 (1998) 112003.
- [14] E155 Collaboration, P.L. Anthony, et al., Phys. Lett. B 493 (2000) 19.
- [15] SMC, B. Adeva, et al., Phys. Rev. D 58 (1998) 112001.
- [16] L.W. Whitlow, et al., Phys. Lett. B 250 (1990) 193;
E143 Collaboration, K. Abe, et al., Phys. Lett. B 452 (1999) 194.
- [17] COMPASS Collaboration, V.Yu. Alexakhin, et al., Phys. Lett. B 647 (2007) 8.
- [18] E.R. Nocera, Phys. Lett. B 742 (2015) 117.
- [19] P. Jimenez-Delgado, A. Accardi and W. Melnitchouk, Phys. Rev. D 89 (2014) 034025.
- [20] E142 Collaboration, P.L. Anthony, et al., Phys. Rev. D 54 (1996) 6620.
- [21] E154 Collaboration, K. Abe, et al., Phys. Rev. Lett. 79 (1997) 26.
- [22] E155 Collaboration, P. L. Anthony, et al., Phys. Lett. B 463 (1999) 339.
- [23] HERMES Collaboration, C. Ackerstaff, et al., Phys. Lett. B 404 (1997) 383.
- [24] R. Machleidt, K. Holinde and C. Elster, Phys. Rept. 149 (1987) 1.
- [25] A.D. Martin, W.J. Stirling, R.S. Thorne and G. Watt, Eur. Phys. J. C 63 (2009) 189.
- [26] A.D. Martin, R.G. Roberts, W.J. Stirling and R.S. Thorne, Eur. Phys. J. C 28 (2003) 455; Phys. Lett. B 604 (2004) 61.
- [27] V. Andrieux, Ph.D. thesis, Université Paris-Sud XI (2014),
<http://www.theses.fr/2014PA112244/document>.
- [28] S. A. Larin, T. van Ritbergen and J.A.M. Vermaseren, Phys. Lett. B 404 (1997) 153.
- [29] J. Beringer, et al., (Particle Data Group), Phys. Rev. D 86 (2012) 010001.